JOURNAL OF PROPULSION AND POWER
Vol. 12, No. 2, March–April 1996

Predicting and Analyzing X-Rays to Measure Propellant Crack Propagation Speed

R. A. Frederick Jr.*
University of Alabama in Huntsville, Huntsville, Alabama 35899
and
B. M. Williams† and S. B. Farmer‡
Sverdrup Technology, Inc., Arnold Air Force Base, Tennessee 37389

Real-time radioscopy (RTR) of solid rocket motors has revealed information about the propellant burning and cracking. This theoretical study evaluated the viability of real-time radioscopy for measuring propellant crack propagation speed. The scope included the quantitative interpretation of crack tip velocity from simulated radiographic images of a burning, center-perforated motor. The simplified motor simulation portrayed a bore crack that moved radially at a speed that was 10 times the propellant burning rate. Comparing the image interpretation with the simulation input quantified the accuracy of the crack velocity measurement under favorable, first-order assumptions. The simulation included the effects of system configuration, finite spatial resolution (from video pixels), and (8-bit) intensity digitization. The image digitization and interpretation introduced a ±20% measurement uncertainty in the crack tip speed for the nominal condition. A ±10% uncertainty resulted from doubling the camera gain. Using curve-fitting techniques, the result was a constant 2% bias in the crack tip velocity measurement. This best case analysis shows that RTR has the potential for making acceptable measurements under the conditions studied.

Nomenclature

a_e = crack ellipse parameter
b_e = crack ellipse parameter
d_1 = propellant thickness under the crack tip
d_2 = propellant thickness under the bore
I = x-ray intensity at the screen
I' = x-ray intensity at the screen center for empty case
I_0 = x-ray intensity at 1 m from the source
l_i = ray path length in the ith material
n = number of materials in object
R_s = distance from source to a point on screen
R_0 = bore radius
R_1 = case inner radius
R_2 = case outer radius
r = propellant burning rate
S = distance of source to motor centerline
T = distance of x-ray screens to motor centerline
t = time from ignition
t_{action} = time the propellant is totally consumed
t_{cw} = time at which the crack tip intersects the case
V_c = velocity of crack tip (fixed coordinate system)
x_e, y_e = center of crack ellipse
x_{min} = screen position representing the inner edge of the bore
Δ_a = strain expansion of crack minor axis, a_e, at $t = 0^+$
Δ_b = strain expansion of crack major axis, b_e, at $t = 0^+$
Δ_0 = strain expansion of bore radius at $t = 0^+$
Δ_1 = strain expansion of case inner radius at $t = 0^+$
Δ_2 = strain expansion of case outer radius at $t = 0^+$
θ = angle from centerline of source
μ_c = linear attenuation coefficient of case
μ_p = linear attenuation coefficient of propellant

Received March 6, 1993; revision received Sept. 6, 1995; accepted for publication Sept. 8, 1995.

*Assistant Professor, Department of Mechanical and Aerospace Engineering. Senior Member AIAA.
†Senior Engineer, Engineering Support Department.
‡Engineer, Plume Data Center.

Introduction

CRACKS in solid-propellant rocket motors sometimes propagate during motor operation causing an increase in pressure that results in a case rupture. The extent of crack propagation can be inferred from the pressure-time trace or examination of extinguished propellant after the case ruptures. Real-time radioscopy (RTR, now used to denote x-ray images recorded on electronic media) has the potential for providing quantitative data on crack propagation during actual motor firings. This study evaluated the limitations introduced by image digitization and interpretation on the measurement of the crack tip velocity. This analysis was motivated by plans to actually test small-scale, intentionally flawed motors to measure propellant crack propagation characteristics using RTR.

Real-time radioscopy of solid rocket motor operation has been used by several agencies over the past 30 years. Wiley[1] described a mobile, real-time system used on the Nike Zeus program in 1964. Other investigators at the U.S. Naval Weapons Center at China Lake,[2] Los Alamos National Laboratory,[3] Arnold Engineering Development Center,[4] and Royal Ordinance[5] have applied this diagnostic approach to various rocket motor applications. Recently, some research work on laboratory-scale motors was reported.[6]

Burning rocket motors present unique challenges in interpreting radiographs because they have continuously changing characteristics that effect the interpretation of the x-rays.[7] The interpretation of the real-time work has remained semiquantitative over the years because the testing conditions degrade the data collection, the cost to include the diagnostics has limited the amount of data, and the self-consuming nature of the event leaves no physical evidence to directly confirm a particular event. Ultimately, most data analyses have been subjective interpretations of the resulting video images.

The point of this work is to address these challenges analytically so that the potential benefits of applying RTR to specific applications can be evaluated and improved. Images were

generated by simulation to provide known inputs and address the self-consuming nature of the real events. This simulated the wide range of exposure level and contrast during a particular test. Algorithms were developed to objectively interpret the resulting images to determine the crack tip propagation speed. This allowed the evaluation of the test configuration and instrumentation setup on the resulting data quality. The approach presented next provides the basis on which other, more realistic features could be included in the simulation such as case expansion, nonlinear transfer functions for the cameras, coupled propellant ballistics, and statistical noise.

Approach

The configuration modeled for acquiring real-time radiographs of an intentionally flawed test motor is shown in Fig. 1. The x-rays are aimed through the motor and then imaged on a fluorescent screen. The screen converts the transmitted radiation into visible light that is recorded by a video camera. An axial crack is oriented so that its depth is collinear with the central ray of the x-ray source. The specifications of the radioscopy setup are listed in Table 1. The analysis of this configuration included developing a simplified model of the propellant movement, predicting the resulting time-dependent x-ray, and determining the crack propagation speed by using an image processor. The basic uncertainties of the image processing techniques were evaluated by comparing the rocket model input and measured results.

The basic assumptions of the simulation include 1) the source emanated from five discrete points, 2) the maximum intensity of the source impinged at the geometrical center of the imaged area, 3) the radiation scattered by the motor was neglected, 4) the source emanated monoenergetic radiation, 5) the imaging screens linearly converted transmitted intensity to visible light without losses, 6) the rocket motor exhibited no axial movement, 7) RTR geometric configuration remained constant, and 8) the camera gain was constant.

Rocket Motor Model

To simplify the image predictions, the rocket motor was modeled using geometric surfaces. Figure 2 shows the end view of the simulated motor. The inner bore, case inner radius, and case outer radius are represented by finite length cylinders having radius R_0, R_1, and R_2, respectively. The crack is represented by an ellipse whose center is at the point x_e, y_e and whose major axis is $2b$ and minor axis is $2a$.

The change in bore and case radius includes components representing the propellant burning rate and a pressure-induced strain:

$$R_0 = (R_0)_0 + \Delta_0 + rt \qquad (0^+ < t \leq t_{action}) \tag{1}$$

$$R_1 = (R_1)_0 + \Delta_1 \qquad (0^+ < t \leq t_{action}) \tag{2}$$

$$R_2 = (R_2)_0 + \Delta_2 \qquad (0^+ < t \leq t_{action}) \tag{3}$$

Although unrealistic, the burning rate was assumed to be constant for all times and places in the motor to simplify the analysis.

The enlargement of the major and minor axis of the crack ellipse was modeled as combination of strain displacement and propellant burn distance

$$a_e = a_{e_0} + \Delta_a + rt \qquad (0^+ < t \leq t_{action}) \tag{4}$$

$$b_e = b_{e_0} + \Delta_b + rt \qquad (0^+ < t \leq t_{action}) \tag{5}$$

The center of the ellipse stays at its initial position. For a propagating crack the major axis of the crack ellipse was assumed to grow

$$b_e = b_{e_0} + \Delta_b + V_c t \qquad (0^+ < t \leq t_{cw}) \tag{6}$$

After this time, the major axis of the ellipse resumes expansion at the propellant burning rate

$$b_e = b_{e_0} + \Delta_b + V_c(t_{cw}) + r(t - t_{cw}) \qquad (t_{cw} < t < t_{action}) \tag{7}$$

until all of the propellant is consumed.

Table 2 lists the particular input parameters assumed for the motor model. The crack represents a flaw that is intentionally cut after the motor is cast. The initial width of the crack models

Table 1 RTR system characteristics

Energy, 100 kV
Output intensity, 75 rad/min
Focal spot size, 0.3 mm
S, 20 in.
T, 6 in.

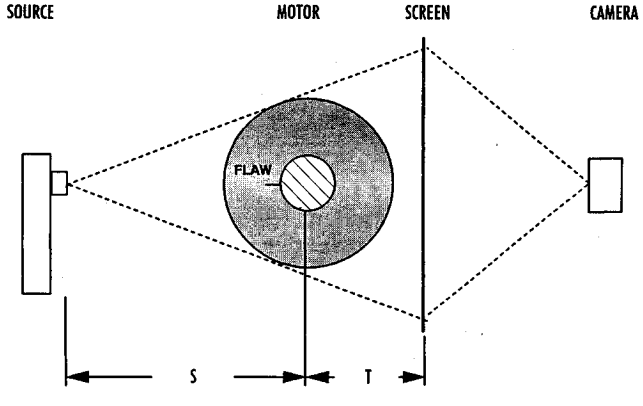

Fig. 1 RTR configuration.

Table 2 Simplified model of case, propellant, and bore crack

Geometric	Operational
$(R_0) = 0.50$ in.	$\Delta_0 = 0.15$ in.
$(R_1) = 2.82$ in.	$\Delta_1 = 0.15$ in.
$(R_2) = 2.88$ in.	$\Delta_2 = 0.15$ in.
$a_e = 0.025$ in.	$\Delta_a = 0.20$ in.
$b_e = 2.82$ in.	$\Delta_b = 0.15$ in.
$x_e = 0.00$ in.	$\mu_p = 0.577$ in.$^{-1}$
$y_e = 0.50$ in.$^{-1}$	$\mu_c = 0.400$ in.$^{-1}$
	$r = 0.5$ in./s
	$V_c = 0.5$ or 5.0 in./s

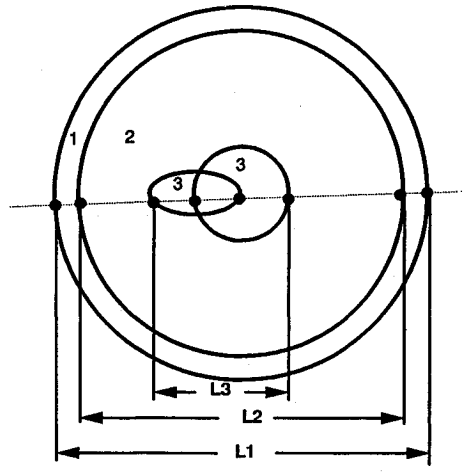

Fig. 2 Geometric surfaces for motor model.

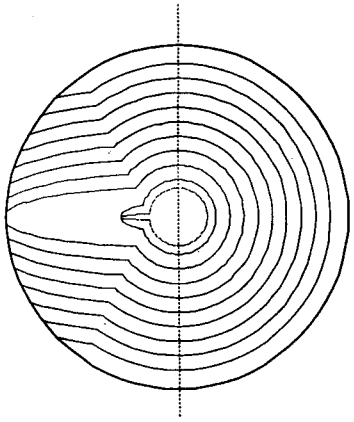

Fig. 3 Propellant burn surface profiles, $\Delta t = 0.5$ s.

the effect of residual thermal strain in the propellant. The crack tip was assumed to propagate at 5.0 in./s (based on a simple finite element calculation). The resulting propellant surface evolution lines, plotted on Fig. 3, show that the crack tip reached the i.d. of the case at 0.36 s from ignition while the remainder of the burning surfaces were constrained to move at 0.5 in./s. This dramatic change in propellant thickness along the radial depth of the crack is the key physical feature that will be used to detect the crack tip velocity.

X-Ray Model

A three-dimensional model[8] was developed to calculate the images for a burning rocket motor. The x-rays originated from five point sources (to simulate a finite size focal spot) and passed through/around finite length geometric shapes. The rays intersect the video screen at 90,000 points (to simulate a 300 by 300 pixel video digitization).

The radiation attenuation model for x-rays being transmitted through an object is based on Beer's law:

$$I = \left(\frac{I_0}{R_s^2}\right) \exp\left(\sum_{i=1}^{n} - \mu_i l_i\right) \tag{8}$$

The radiation that reaches each point on the screen is determined by calculating the length l_i of each material through which a ray passes, knowing the linear attenuation coefficient for each material, and the distance of the source to the screen intersection R_s. These distances were determined from the intersection points of each ray with the geometric shapes that represented the case and propellant surfaces. The conversion of the transmitted radiation incident on the screen into a video signal was assumed to be a linear process.

Image Generation/Analysis

A RISC-based IBM workstation calculated the transmitted intensity at the screens for 1/30 s time steps from motor ignition to burn out. The ray-tracing model was applied to the specific motor geometry to predict the transmitted intensity reaching the screens. The computer converted the screen intensity to digital gray levels by simulating an 8-bit digitizer (0–256). The gray level at each point of a 300 by 300 pixel (8-bit) image file was then calculated for each time step and saved electronically on disk.

For analysis the image files were called into an image processor. The image processor extracted radial intensity profiles from the picture files for data interpretation. This allowed algorithms to be implemented on the analysis hardware with images that were generated digitally, rather than from an actual test. Image processing routines were ultimately refined to an automated mode to determine the crack tip propagation speed.

The fundamental approach for determining crack velocity relies on making a calibrated, intensity measurement of the

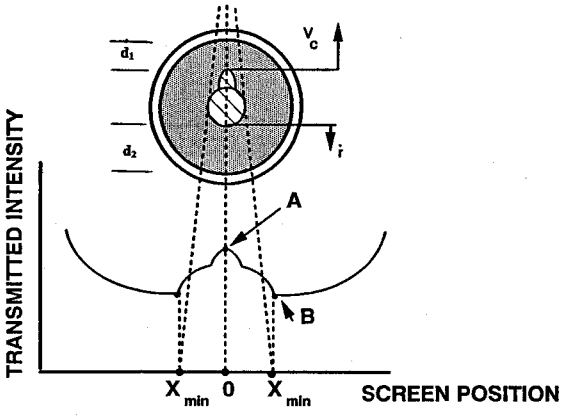

Fig. 4 Important considerations for analysis.

radiation transmitted through the crack tip. Figure 4 is a sketch of the motor and the resulting transmitted radial intensity profile. Since the propellant is the only material that changes path length during motor operation, the maximum transmitted intensity is

$$I_A = I' \exp[-\mu_p(d_1 + d_2)] \tag{9}$$

The change in propellant path length along this ray $\Delta d = \Delta d_1 + \Delta d_2$, over a time interval $t_2 - t_1$, is

$$\Delta d = -[R_0(t_2) - R_0(t_1)] - [V_c(t_2 - t_1)] \tag{10}$$

which is also related to the change in transmitted intensity

$$\Delta d = -(1/\mu_p)\ell n[I(t_2)/I(t_1)] \tag{11}$$

if the offset of the system electronics is zero. In practice the offset would be determined from a known motor configuration (i.e., prior to motor ignition) and subtracted from the intensity values used in Eq. (9).

Combining Eqs. (10) and (11), the sum of the crack tip velocity and the propellant burning rate propagation over a finite time interval is

$$V_c + r = \frac{(1/\mu)\ell n[I(t_2)/I(t_1)]}{(t_2 - t_1)} \tag{12}$$

To apply this equation to determine the crack tip velocity, it is necessary to determine 1) the centerline transmitted intensity and 2) the propellant burn rate as a function of time.

The propellant burning rate can be determined from the edge features of the transmitted radiation profiles. Since the maximum x-ray path length through the motor is tangent to the bore, the measured position of the intensity minimum (point B in Fig. 4) represents the bore radius

$$R_0(t_i) = \frac{Sx_{\min,i}}{[(S+T)^2 + (x_{\min,i})^2]^{1/2}} \tag{13}$$

Substituting Eq. (13) into Eq. (12), a finite divided difference formula for the average velocity of crack propagation between times t_2 and t_1 results as

$$V_c = \frac{\frac{1}{\mu_p}\ell n\left[\frac{I(t_2)}{I(t_1)}\right]}{(t_2 - t_1)} + \frac{\left\{\frac{Sx_{\min,2}}{[(S+T)^2 + (x_{\min,2})^2]^{1/2}} - \frac{Sx_{\min,1}}{[(S+T)^2 + (x_{\min,1})^2]^{1/2}}\right\}}{(t_2 - t_1)} \tag{14}$$

Results and Discussion

Images Simulation

Example radioscopic predictions are shown in Fig. 5. The side view looking along the radial depth of the crack is shown in Fig. 5a. The inner edge of the bore is visible above and below the centerline of the motor. The crack is also discernible as a lighter strip running the length of the motor along its centerline. Figure 5b shows a predicted image for x-rays being transmitted from the front to the back of the motor. This photo represents the same instance in time as Fig. 5a. It is used to better illustrate the condition of the crack at this instant of time.

Although visually, the end view provides an almost direct image of the grain and crack tip profile, it might not be a practical approach for data collection. First, motor hardware such as the thrust adapter and nozzle would impair such a view. Second, the crack tip is not expected to travel at a constant velocity along the length of the motor so that this view would be unable to resolve the axial variations.

Image Analysis

Figure 6 shows the radial screen intensity profiles at selected times. The left half of the graph represents the scenario of no crack tip propagation while the right half of the graph represents 5 in./s tip propagation. The motor expansion on initial pressurization is indicated by the radial change between the $t = 0$ (dotted) and the $t = 0^+$ (solid) lines. The x location of the minimum points on each curve defines the bore radius by Eq. (13).

The intensity levels of the radial profiles suggest that cameras could sense the image in practice. Experience has shown[8] that an intensity level of about 1 rad/min at the screens is required for an image to be detected by the cameras. The intensity in Fig. 6 is in integer gray levels, which is the form that test data are digitized for analysis. For the model used here, one gray level represents a value of 0.67 rad/min at the screen which is dependent on measurement system gain and offset. Using these conditions modeled, the minimum radiation levels are above the threshold values at 4 rad/min.

A computer algorithm determined the radial location of minimum intensity level at each time step. Because of the low contrast at the bore and the finite number of intensity levels, the minimum was not a single point. The minimum intensity level actually spanned several pixels (in the radial direction). In previous work,[9] the middle pixel on this plateau was selected as the bore edge. This was shown to produce a consistent bias. That algorithm has been improved to use the innermost pixel (closest to motor centerline) rather than the midpoint of the minimum pixel plateau. Because of the sharper intensity gradient at the bore, this gives the most accurate results. The spatial digitization attributable to simulating 300 discrete video lines resulted in a 0.04-in. distance resolution at the x-ray screen. This translates to approximately 0.03-in. resolution of the bore radius.

Figure 7 shows the peak transmitted intensity as a function of time for the 5-in./s propagating crack. The simulated data points are calculated at intervals of 1/30 of a second corresponding to the video camera frame rate. The curves are exponential fits. When the crack intersects the case at t_{cw} a discontinuity in the intensity-time curve is seen. The average crack velocity between ignition and this time could be calculated by simply dividing the difference in case radius and initial crack tip radius by t_{cw}.

Image Evaluation

Figure 8 shows three curves for the propagating crack tip: 1) the total air gap curve ($R_0 + y_e + b_e$) determined from the transmitted intensity data (Fig. 7), 2) the bore radius determined from analysis of the local minimums of the intensity profiles, and 3) the crack tip radius (determined by subtracting 2 from 1). The slope of curve c is the crack propagation velocity. Digitized points are represented by symbols and the lines are curve fits of the calculated data points.

Figure 9 is a plot of the resulting crack tip velocity as a function of time. The horizontal line at 5.0 in./s represents the crack tip speed modeled in the motor simulation. The uneven line oscillating about this connects the velocity points deter-

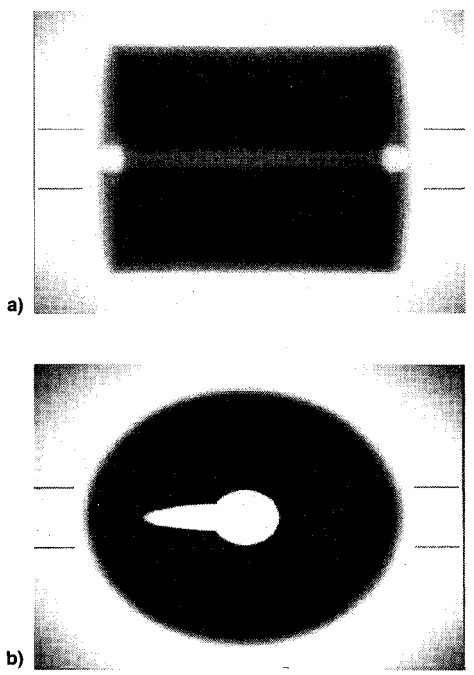

Fig. 5 Predicted images.

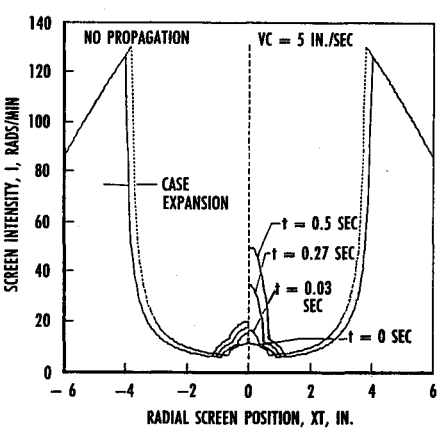

Fig. 6 Predicted radial intensity profiles.

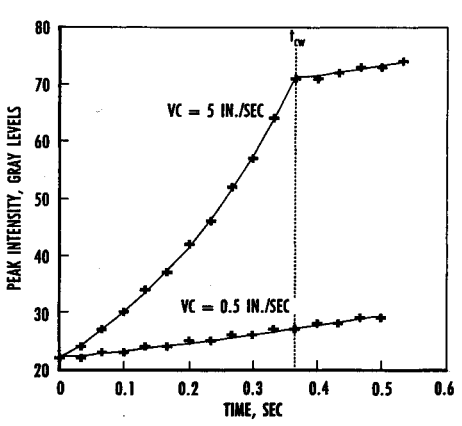

Fig. 7 Centerline intensity.

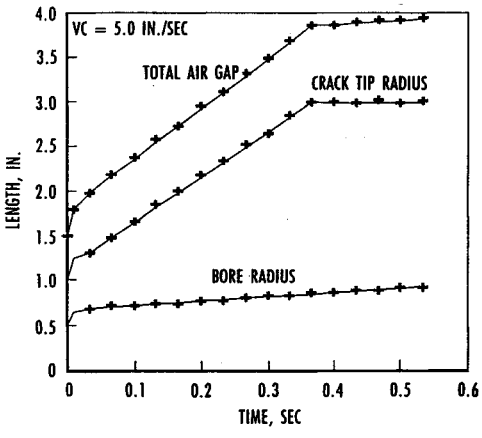

Fig. 8 Measured displacements.

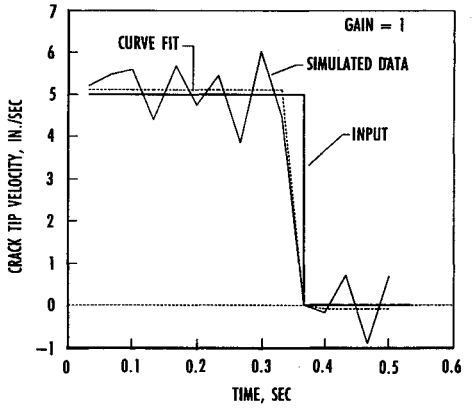

Fig. 9 Crack tip velocity, gain = 1.

mined by the finite divided difference evaluation. This oscillation has a maximum excursion of ±1.0 in./s that results from two components. The first is the 0.30-in. spatial resolution in the measurement of the bore radius. The second is the discrete intensity levels in the digitized transmitted intensity. Using the curve-fit analyses of the predicted intensity and bore radius (Figs. 7 and 8) produces a consistent bias in the crack tip velocity of 0.1 in./s as shown by the dashed line in Fig. 9. The uncertainties are then ±20% for the finite divided difference analysis and ±2% for the curve-fitting analysis when normalized to the nominal crack tip speed.

Since the camera gain [camera gain is the relation for converting screen intensity (rad/min) to picture gray levels (0–255)] will influence the intensity resolution, an increase in camera gain was evaluated. Increasing the camera gain allows the intensity changes to span more gray levels. The results of the finite divided difference analysis had a maximum error of ±0.6 in./s, whereas the curve-fit data had a constant bias of +0.06 in./s. This shows how setting camera gains prior to motor testing can improve the accuracy of the results.

Other system-level considerations may preclude camera gain increases to avoid video saturation in another part of the image. A practical approach would be to monitor the automatic gain control on the camera and include it in the analysis of the transmitted intensity measurements.

Benefits and Limitations of the Model

The point of the study was to determine if the crack velocity measurement was possible under best-case assumptions. If not, then a major change in diagnostic approach would be required. Since this analysis indicates that the measurement is viable, further refinements of the model are now warranted. In its present form, the model can assist in the design of test configurations that could minimize the measurement uncertainty associated with the digital imaging for particular flaw scenarios. The interactions among camera gain, source/screen position, motor orientation, and image processing algorithms can be modeled to suggest configurations that improve measurement accuracy.

Other factors are important when evaluating RTR for crack tip velocity measurements. The camera and screen have threshold detection levels and nonlinear gains.[10] Other considerations include a more detailed structural/ballistic model of the rocket motor, the output energy intensity distribution of the source, effects of video noise, and fogging from scattered radiation. The real-time data is typically noisy suggesting that the robustness of the present approach must now be evaluated in the presence of fluctuating intensity levels. Using the methodology presented, it is possible to evaluate the effects of these phenomena on the system.

Conclusions

This modeling has demonstrated a methodology for evaluating and improving the accuracy of crack tip velocity measurements for RTR. Video digitization resulted in a measurement uncertainty of ±20% for a crack traveling at 5.0 in./s. The simulations showed that this uncertainty can be reduced to ±10% in./s by doubling the camera gain. Using a curve-fit analysis reduced the uncertainty to 2%. While not all of the practical effects of the motor and diagnostic systems are modeled, the methodology shows that by using the best-case assumptions for the simulation, a useful measurement of crack tip speed is possible. Since this is true, the approach merits further analytical and experimental consideration.

References

[1]Wiley, R. G., "Photo Recording Internal Ballistics and Flame Fronts of Solid Propellant Engines by Cine-X Data Process," *Proceedings of the 9th Annual Technical Symposium of SPIE* (Miami Beach, FL), International Society for Optical Engineering, Bellingham, WA, 1964.

[2]Rogerson, D. J., "Dynamic Real-Time Radiography of Solid Propellant Rocket Motors During Static Firing," *Materials Evaluation*, Vol. 45, Nov. 1987, pp. 1330–1333.

[3]Fackrell, F. N., "Aft Dome Internal Insulation Erosion on SICBM Pre-FSD Stage I Solid Propellant Rocket Motors," AIAA Paper 90-2324, July 1990.

[4]Belz, R. A., Girate, P. T., Walker, R. Y., Nichols, J. A., and Bapty, T. A., "Radiographic Diagnostics for Tactical Missile Development," *JANNAF Propulsion Meeting*, Chemical Propulsion Information Agency, CPIA Publication 480, Vol. 1, 1987, pp. 47–55.

[5]Aytis, J., and Petrovic, S., "Erosive Burning in Solid Propellant Rocket Motors," AIAA Paper 90-2215, July 1990.

[6]Hsieh, W. H., Char, J. M., Zanotti, C., and Kuo, K., "Erosive and Strand Burning of Stick Propellants, Part I: Measurements of Burning Rates and Thermal Wave Structures," *Journal of Propulsion and Power*, Vol. 6, No. 4, 1990, pp. 392–399.

[7]Williams, B. M., and Frederick, R. A., Jr., "Predicting X-Ray Images for Dynamic Flaw Detection," 1991 JANNAF Propulsion Systems Hazards Subcommittee Meeting, March 1991.

[8]McAmis, R. W., Williams, B. M., Anderson, M. G., Barnes, D. M., and Farmer, S. B., "Predicting Dynamic Radiographic Images in Solid-Propellant Rocket Motors," AIAA Paper 95-2593, July 1995.

[9]Frederick, R. A., Williams, B. M., Bain, J. C., and Nichols, J. A., "Predicting X-Ray Images for Burning Solid-Propellant Rocket Motors," AIAA Paper 91-0305, Jan. 1991.

[10]Walker, R. Y., Moyers, R. L., and Anderson, M. G., "Comparison of X-Ray-to-Light Conversion Devices for Real-Time Radiography Applications," Chemical Propulsion Information Agency, CPIA Publication 616, Oct. 1994, pp. 25–32.